

Real-time closed-loop tissue-specific laser osteotomy using deep-learning-assisted optical coherence tomography

YAKUB. A. BAYHAQI,¹  ARSHAM HAMIDI,¹  ALEXANDER A. NAVARINI,² PHILIPPE C. CATTIN,³  FERDA CANBAZ,¹  AND AZHAR ZAM^{1,4,5,*} 

¹Biomedical Laser and Optics Group (BLOG), Department of Biomedical Engineering, University of Basel, 4123 Allschwil, Switzerland

²Digital Dermatology Group, Department of Biomedical Engineering, University of Basel, 4123 Allschwil, Switzerland

³Center for medical Image Analysis and Navigation (CIAN), Department of Biomedical Engineering, University of Basel, 4123 Allschwil, Switzerland

⁴Division of Engineering, New York University Abu Dhabi, Abu Dhabi, 129188, United Arab Emirates

⁵Tandon School of Engineering, New York University, Brooklyn, NY, 11201, USA

*azhar.zam@nyu.edu

Abstract: This article presents a real-time noninvasive method for detecting bone and bone marrow in laser osteotomy. This is the first optical coherence tomography (OCT) implementation as an online feedback system for laser osteotomy. A deep-learning model has been trained to identify tissue types during laser ablation with a test accuracy of 96.28 %. For the hole ablation experiments, the average maximum depth of perforation and volume loss was 0.216 mm and 0.077 mm³, respectively. The contactless nature of OCT with the reported performance shows that it is becoming more feasible to utilize it as a real-time feedback system for laser osteotomy.

© 2023 Optica Publishing Group under the terms of the [Optica Open Access Publishing Agreement](#)

1. Introduction

Over the last decades, laser technologies for cutting bones have developed rapidly. Lasers produce a cleaner surface cut, cause fewer mechanical vibrations, offer more flexible cutting geometries, cause fewer material losses, and show less microorganism contamination than conventional saws, drills, or burs [1–7]. Laser osteotomy, especially with *erbium-doped yttrium aluminium garnet* (Er:YAG) laser, is ideal for efficient bone ablation with very little carbonization [8–13]. However, similarly to mechanical tools, there is an inherent risk of collateral damage to surrounding tissue, such as bone marrow and nerves. This remains a challenge in laser osteotomy, especially over the ablation direction. In osteotomy with mechanical tools, physical feedback (i.e., haptic feedback) helps surgeons to stop cutting as soon as some damage is done to the bone marrow so that the risk of cutting nerves is avoided. Controlling the laser osteotomy is also difficult. Ideally, a surgeon plans the ablation site and depth based on the patient's computed tomography (CT) data. The ablation depth could be simply calculated from the ablation rate per pulse. Nevertheless, the accuracy of such a process is limited to the resolution of the CT and the ablation rate calculation. The ablation rate is influenced by multiple factors, such as the shape of the laser beam, the energy per pulse, the cooling system, the tissue density, and the water content [13–15].

One solution to this problem is to integrate a closed-loop control system that would make it possible to safely perform laser osteotomy without damaging critical internal tissues. Researchers have sought to address this issue throughout the last decade. Such a control mechanism aims to identify tissue type below the laser-ablated incision during the cutting process. The ablation process would be terminated as soon as soft tissue (such as bone marrow or nerves) is detected.

Such a detection system can be achieved by analyzing the secondary light and the acoustic emission produced by the laser's interaction with tissue or by integrating the ablation laser with additional diagnostic modalities.

Analysis of secondary light emissions includes random lasing (RL) [16] and laser-induced breakdown spectroscopy (LIBS) [17–21], which have been demonstrated to be promising methods for differentiating tissue types. It has been shown that RL has nanoscale sensitivity to small structural changes [16]. LIBS could run under operating room light and has a very high accuracy for tissue differentiation at an atomic scale [18,19,22]. Even more, LIBS could also be used for carbonization detection [23], preventing permanent damage to the bone. But each of these methods also has its own disadvantages. RL depends on a laser dye that might harm biological tissue, while LIBS has limitations in reaching a deep cut and is more accurate for characterizing tissue surfaces. Furthermore, research in analyzing the acoustic signals emitted by photoablation (ablative optoacoustic techniques) has also been demonstrated to have comparable accuracy [24–28]. These methods require, however, a high-energy pulsed laser to produce a measurable acoustic signal; thus, damage to the tissue is almost unavoidable.

Another interesting method for analyzing the effects of photoablation was presented by Rupprecht *et al.* [29,30]. Their approach combines analyzing both secondary light emissions and acoustic signals (combined pyrolysis-photoacoustic). Here, the light emission from the pyrolysis process in the ablation zone is observed with a photodiode. At the same time, a piezoelectric accelerometer is used to measure the generated acoustic signal. The measured signals were used to interrupt the laser beam as soon as threshold values were reached. Additionally, we could also use the pyrolysis signal for detecting bone carbonization [31]. However, this method inherits similar drawbacks from the previously mentioned methods. A high-energy pulsed laser is needed to generate the pyrolysis light. Even more, the piezoelectric accelerometer needs to be mounted to the bone, which causes unnecessary damage.

Contactless laser ablation can be integrated with additional nonimaging and nonablating diagnostic modalities. Raman spectroscopy [32,33] provides information regarding the molecular bonds of tissue and has a high accuracy comparable to LIBS. However, a few seconds of integration time is required to get an observable signal [32], which makes it unsuitable for a real-time feedback system. Another alternative, autofluorescence [34,35] and diffuse reflectance spectroscopy [36–39], may be used to differentiate tissue types with a faster processing time. But these techniques work as a point measurement, thus lacking structural information about the tissue anatomy over the depth.

Among the methods previously mentioned, to date, only LIBS [21] and the combined pyrolysis-photoacoustic [29,30] methods have been experimentally tested for use in a real-time closed-loop control system for laser osteotomy. However, although both methods have high accuracy, these methods distinguish tissue type only after an ablation pulse has been applied, which increases the risk of collateral damage during laser ablation. A further drawback of these approaches is that they can only detect tissue transitions after crossing the tissue boundary. Damage to critical structures is thus almost unavoidable.

We proposed a contactless and ablation-free optical coherence tomography (OCT) imaging system for monitoring the laser ablation process. This emerging imaging technology is analogous to ultrasound imaging that performs noninvasive cross-sectional tomography using light propagation in media and interference phenomena. The echo time delay of the back-reflected or backscattered light from the tissue's internal microstructures is measured using interferometry of partially coherent light. It has been demonstrated as a viable alternative to ultrasound for real-time, high-resolution, and in situ investigations of thin tissue structures [40–42]. This noninvasive imaging modality depicts not only a topological profile of the examined surface but also displays the subsurface structures [43,44]. It has become a standard technique in ophthalmology for

diagnosing retinal diseases [45,46]. Additionally, over the last decades, OCT has become an alternative to ultrasound for intravenous imaging [47–51].

OCT has been employed in several studies to obtain subsurface information from different tissue types and has been used as guidance for laser-ablation surgery, including in tumor resection [52,53], cochlear implant surgery [54,55], and bone osteotomy [56–58]. Increases in resection accuracy and precision for brain tumors and blood coagulation have been reported as advantages of utilizing this technology [52,53,59]. One study showed that OCT helps to shape the endosteal layer's curvature for cochlear implantation with a mean absolute accuracy of around 20 μm [54]. Moreover, some literature has demonstrated that OCT could also be used to monitor the relative temperature of the ablated bone surface, enabling the prevention of bone carbonization [60,61]. Specifically, OCT has been tested as a noncontact real-time feedback system for monitoring the ablation depth of a laser in controlled bone osteotomy [56–58]. Nevertheless, these approaches mainly focus on measuring the position of the target tissue (depth control).

In this work, we utilized OCT to guide the laser osteotomy by detecting tissue type based on the OCT image and providing real-time feedback. Specifically, our proposed method takes advantage of deep learning algorithm to identify the tissue types because it could provide an efficient and accurate way to differentiate tissue. Thus supporting our real-time feedback system. To the best of our knowledge, this is the first approach to provide the basic framework for a real-time closed-loop tissue-specific feedback system based on OCT. In the present study, we focused on testing the performance of the feedback system in differentiating bone and bone marrow in real-time. The experiments were done on fresh porcine femur bones with bone marrow inside. The primary objective of the tissue-specific feedback system was to cut the bone and to stop the laser ablation whenever bone marrow was detected. In the future, we foresee optimizing the feedback system for more precise predictions and more tissue types.

2. Methodology

2.1. OCT closed-loop controlled-laser-ablation setup

An Er:YAG (Syneron LiteTouch, Israel) ablation laser was used for our laser-osteotomy study because of its efficient ablation rates and low carbonization effect [8–13]. The ablation laser's wavelength (2.94 μm) is strongly absorbed by both water and hydroxyapatite, which are the main components of bone. The absorption of such laser light leads to photothermal ablation [1,10]. The irradiated area consequently experiences heat transfer and an increase in pressure. The tremendous build-up of pressure in a fraction of microseconds induces the explosion of tissue material at the focal-spot area. Such heat transfer may rapidly increase the temperature in the surrounding area and lead to carbonization outside the focal spot. A water spray and pressurized air are usually used to keep the temperature of tissue below the carbonization threshold. Rehydrating the tissue also increases its water content and improves the ablation rate.

The closed-loop controlled-laser osteotomy aims to provide detection of the tissue types encountered during laser ablation to avoid cutting critical tissues. Our concept of OCT closed-loop controlled-laser ablation is illustrated in Fig. 1(a). The Er:YAG laser beam was focused on the bone surface by a CaF_2 lens (L3) with a focal length of $f = 75$ mm. The ablation laser and the OCT system were coaxially coupled with the help of a dichroic filter (DF) [Advanced Osteotomy Tools II-VI 80048151, Switzerland]. A sapphire window with a 2 mm thickness was placed in front of the filter to protect the optical components from debris and water droplets splashing around during ablation. Additionally, pressurized air was used to deflect the debris trajectory to prevent bone debris from accumulating on the sapphire window, which could reduce the incident energy of the laser and deteriorate the OCT image.

We used a custom long-range Fourier-domain OCT system with an extended depth of focus for deep-ablation monitoring. It was equipped with a laser source (Insight Photonic Solution, Inc., Lafayette, Co, USA) with a central wavelength of 1310 nm, a spectral bandwidth of 61.5 nm, and

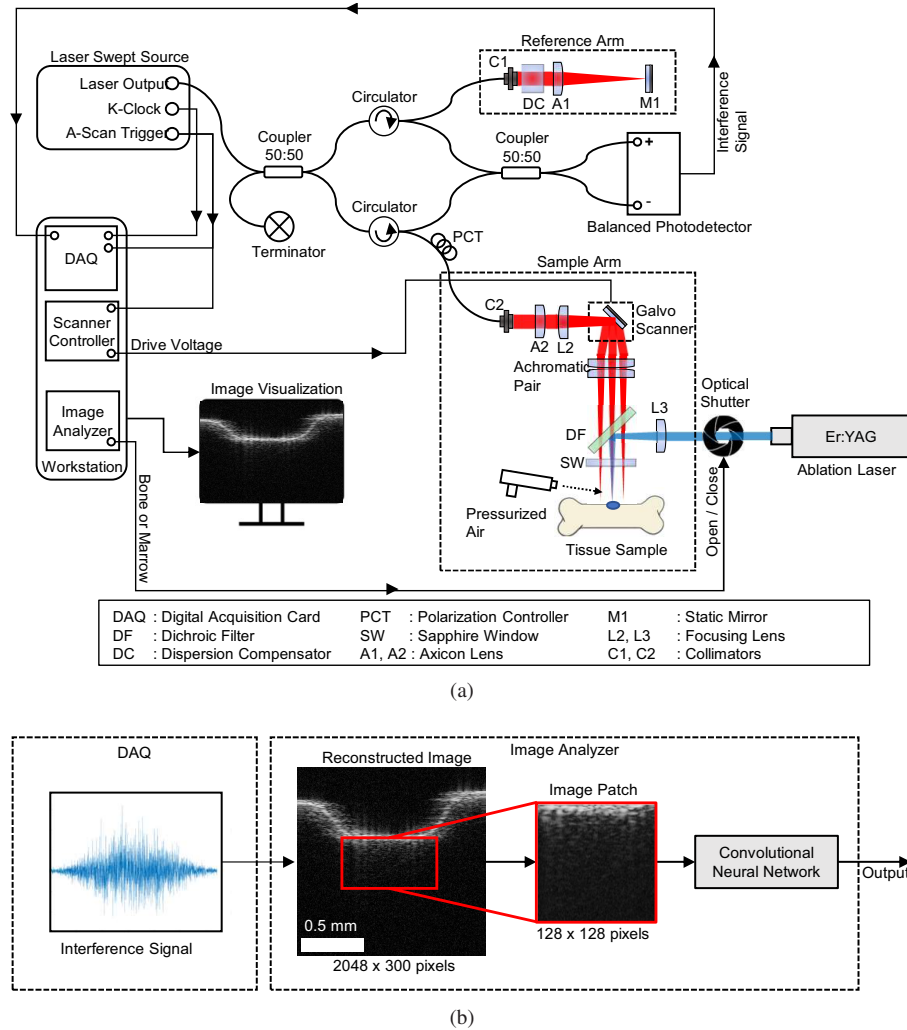


Fig. 1. (a) Schematic of the proposed OCT-based closed-loop controlled-laser osteotomy. We used a custom long-range Fourier-domain OCT with a Bessel-like beam (BLB) optical setup [39]. A dichroic filter coupled the OCT (red line) with an ablation laser (blue line). The OCT images were analyzed (image analyzer) to identify the ablated tissue type. The output provided feedback to an optical shutter that controlled the ablation laser to either stop or continue ablation. (b) The image analyzer worked based on an image patch. A region of interest (image patch) from the OCT image was selected on the ablation spot. We trained a convolutional neural-network model to identify the tissue type based on the extracted image patch.

an A-scan line rate of 104.17 kHz. The OCT system had an imaging range of 26.2 mm in the air. The long-range imaging ability was achieved using a Bessel-like beam (BLB) optical setup, as explained in our previous publication [42]. The reconstructed B-scan images from the OCT system had the dimensions of 2048 pixels (26.2 mm) in the axial and 300 pixels (1.5 mm) in the lateral direction. The corresponding lateral and axial resolutions were $26\ \mu\text{m}$ and $18\ \mu\text{m}$, respectively. The sensitivity or the maximum signal to noise ratio (SNR_{max}) of the OCT system was 110 dB. The OCT system was controlled with a workstation that was equipped with an Intel Core i9-7900X

central processing unit (CPU) and an NVIDIA GTX 1080Ti graphics processing unit (GPU). The interference signal was detected by a balanced photodetector (Thorlabs PDB48xC-AC, Germany) and digitized by a PCIe Waveform Digitizer (Alazartech ATS9373, Canada). OCT images were reconstructed from the interference signal through several preprocessing steps such as Direct Current (DC) subtraction, windowing, zero padding, and inverse Fourier transformation. All of this signal processing and image reconstructions was calculated on the GPU using the compute unified device architecture (CUDA) library for fast parallel processing [62].

The OCT images were streamed to monitor the ablation process. The detection system worked based on an image patch taken from the ablation area (see Fig. 1(b)). The patch was used as a deep-learning model input to discriminate between tissue types. In this paper, the deep-learning model was trained to differentiate between bone and bone marrow (see Section 2.3). The model's output provided feedback to an optical shutter (Thorlabs SH1, Germany) for indirectly controlling the Er:YAG ablation laser.

2.2. OCT scan pattern

The Er:YAG laser circular beam at the surface of the bone tissue had an estimated diameter of ~ 1.0 mm with beam quality factor $M^2 = 22$. Meanwhile, the lateral resolution of the OCT image was $20\text{ }\mu\text{m}$, so a significant area of ablation was not covered by a single B-Scan image, see Fig. 2. Our proposed approach for detecting tissue type was based on detecting three image patches from three different scan locations (images) over the monitored ablation hole. The number of locations was chosen as a trade-off between acquisition time and coverage of the ablation area. This scanning mechanism is illustrated in Fig. 2. In total, nine B-scan frames were acquired for every detection step, which corresponds to an acquisition rate of 28.94 Hz (34.56 msec). For each scan location, the image was frame-averaged from three consecutive B-Scan frames to obtain better quality images. The tissue type of the monitored ablation crater was determined by detecting three image patches from three scan locations simultaneously and taking the majority voting of the detection results.

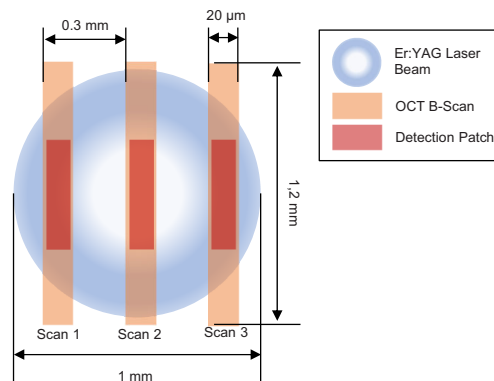


Fig. 2. Top-view illustration of the OCT scan pattern (orange) to cover the bigger area of the Er:YAG laser beam. The color gradation from white (higher) to blue (lower) indicates the intensity (fluence) of the laser beam. Our detection approach involved three detection locations (red) that corresponded to analyzing three OCT B-scan images simultaneously.

2.3. Tissue differentiation

Tissue detection or classification has most recently been the research focus in clinical applications of OCT, such as retinal diseases [63], cancer [64], or atherosclerosis plaque detection [47].

Conventionally, tissue detection has usually been done by discriminating the feature representation (such as attenuation coefficient and textural features) of the tissue in the OCT image. Discrimination using machine learning algorithms, such as random forest (RF) [47], principle component analysis (PCA), and support vector machine (SVM) [64] have been demonstrated to be useful and have shown good accuracy for automatic tissue differentiation. However, the complicated feature extraction of the image increased the prediction time, which is a critical point for a real-time feedback system. As an illustration, the method proposed by Ughi *et al.* [63] in 2013 took about 2 seconds to detect the atherosclerotic plaque using the attenuation estimation and RF classification algorithm. Another example was done by Müller *et al.* [64] in 2021. They needed 1.6 seconds to automatically classify tissue in brain metastases using textural features and SVM.

Currently, one of the most popular methods for image recognition is by using deep learning algorithms, specifically the convolutional neural network (CNN). As one of the deep-learning models, CNN has been known to have better accuracy and efficiency for object detection on an image than other classical machine-learning methods or even other traditional deep-learning models such as multi-layer perceptron (MLP) [65,66]. The convolutional layer of CNN operates as spatial filters that extract high-level features such as edges from the input image.

In OCT research, CNN was proposed as an alternative for real-time image recognition because of the non-complicated or straightforward feature extraction for recognizing the patterns of specific tissues in OCT images. In 2017, Roy *et al.* developed ReLayNet [67] which is able to segment retinal layers in 10 msec. Followed by Borkovkina *et al.* in 2020 [68], they have successfully accelerated the segmentation of retinal layers to only 3.5 msec.

Moreover, in our previous experiments [69], CNN models such as VGG [70], ResNet [71], and DenseNet [72] were demonstrated to have an accuracy of more than 90 % to differentiate five tissue types with an inference time of less than 65 msec. We found that DenseNet has better accuracy compared to the other tested models. Specifically, we have demonstrated that this model had an accuracy of 91.52 % with an inference time of 52.73 msec. Therefore we chose DenseNet (DenseNet121) as the tissue-classifier model for the present experiments.

In this work, we modified the DenseNet model output to recognize bone and bone marrow. The input of the DenseNet model is an image patch that was selected in such a way as to represent a region of interest where a destructive laser pulse would be applied. Technically, the ablation spot is fixed in the lateral center of the B-scan image. Before conducting the experiments, the OCT was aligned such that the B-scan image is centered to the hole ablation, as illustrated in Fig. 1(b). The tissue surface in the B-scan image was detected using the vertical Canny edge detection method because of its simplicity and low sensitivity to noise [73,74]. A square of 128 pixels \times 128 pixels area was extracted from the ablation spot and defined as the input patch for the DenseNet model. Examples of the image patches are shown in Fig. 4. Finally, the model had two outputs with sigmoid activation function, which gave the tissue-type prediction (bone or bone marrow).

2.4. Training, testing, and online inference

The data sets used to train the DenseNet model were taken from ex-vivo pig-bone samples. The samples were acquired from a local butcher. Specifically, the samples were taken from the middle section of the femur bone and consisted of the compact bone as the outer layer and the bone marrow inside. The muscle and connective layer were removed before the experiments. For fully supervised training, the bone image patches were taken from the bone surface, while the bone marrow image patches were taken from the sample's side, as illustrated in Fig. 3(a) (blue line for bone and red line for bone marrow).

There are, however, some challenges for tissue classifiers during laser ablation. The tissue experiences an increase in temperature (heating up) during microsecond ablation. This will

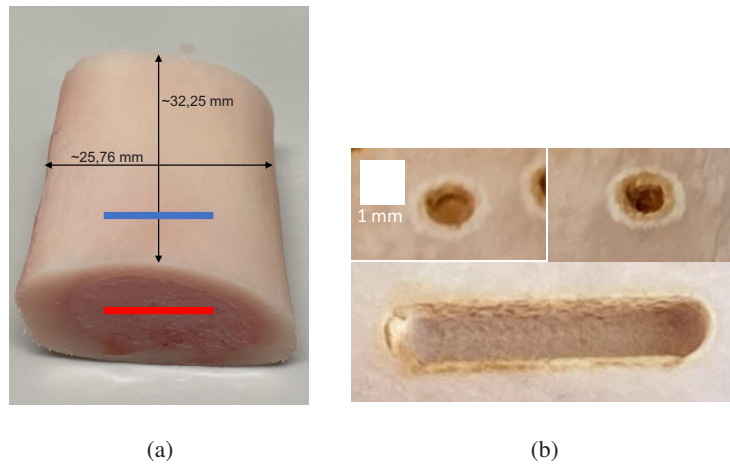


Fig. 3. (a) Example of a pig femur bone sample used in the experiment with bone marrow inside. The OCT B-scan images, used for deep learning training, were scanned at the blue line for bone tissue and at the red line for bone marrow. The average thickness of the bone layer was 2.5 mm. (b) Example of the dehydrated bone after receiving 12-18 laser pulses. The top images show bone dehydration with hole ablations. The bottom image shows bone dehydration with a line ablation. The hole-ablated bone experiences more dehydration to carbonization (indicated with a darker color) than the line-ablated bone, because it better distributed the heat from the laser (See section Section 2.5).

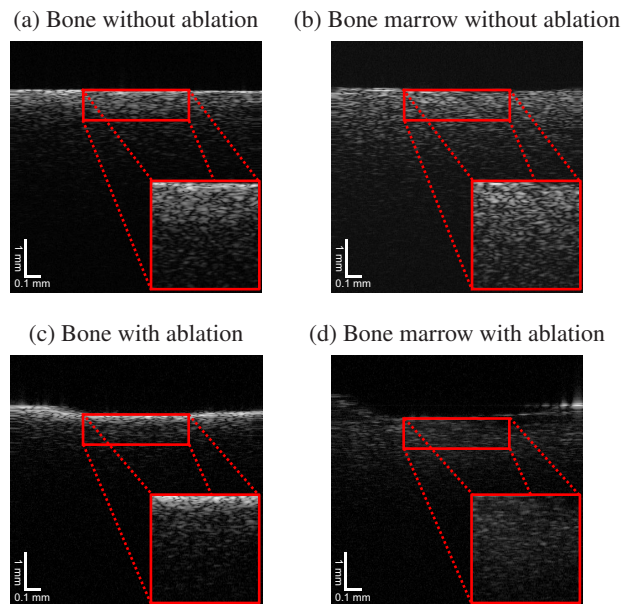


Fig. 4. Examples of OCT B-scan images collected in the experiment. Bone (a) and bone marrow (b) images without laser ablation. Bone (c) and bone marrow (d) images during laser ablation with 200 mJ. The image of bone during ablation shows an increase in intensity due to water dehydration. By contrast, the image of bone marrow shows a decrease in intensity due to light absorption by liquid materials at the surface.

induced dehydration to the bone as shown in Fig. 3(b). As a consequence, the optical properties of the tissue (such as the refractive index, absorption coefficient, and scattering coefficient) change [35,37]. These changes affect the textural information in the OCT images and may reduce the tissue classifier's accuracy. For these reasons, we trained the classifier using image patches from four different conditions. The first patches were taken without applying the laser. The other patches were taken while applying the ablation pulses with the energy of 200, 150, and 110 mJ, respectively.

Five pigs, with three samples from each pig, were used to train and test the classifier. As explained in the previous paragraph, image patches from each sample were taken from four ablation conditions, with 1000 image patches per ablation condition. Thus, a total of 8000 image patches consisting of 4000 image patches of bone tissue and 4000 image patches of bone marrow were collected for each sample. The samples were separated into six samples from two pigs for training, three samples from one pig for validation, and six samples from two pigs for testing. In other words, the data sets were separated into 48,000 (24,000 per tissue) patches for training, 24,000 (12,000 per tissue) for validations, and 48,000 (24,000 per tissue) for testing the DenseNet model.

The training of the DenseNet model was implemented using the Pytorch Deep Learning framework [75]. We trained it on an NVIDIA DGX A100 workstation equipped with NVIDIA A100 GPUs, which enabled us to perform parallel computations to speed up the training process. The model was trained with 1000 epochs and a batch size of 32 samples. We defined cross entropy as the training loss function and Adam (learning rate = 1.0×10^{-4}) as the training optimizer. Furthermore, we performed data augmentation to the patch image during training by random small shifts and horizontal flips.

The inference of the DenseNet model was done on the OCT workstation and embedded as one of the processing pipelines. After training the DenseNet model in Pytorch, we converted the model to the Open Neural Network Exchange (ONNX) format [76], which can be read by the NVIDIA TensorRT [77] library for parallel deep-learning inference in our OCT's GPU. This inference mechanism performed faster than previously reported inference mechanisms [69]. TensorRT ran the model inference in a parallel programming manner inside the NVIDIA GPU and used the GPU's memory to hold the input patch of the model. In our system, the OCT signals were processed in the GPU. Thus, the reconstructed images already resided in the GPU's memory. Copying the OCT-reconstructed image to the DenseNet-model input was also done in the GPU. We thus avoided unnecessary memory copy between the CPU and the GPU. The inference of our DenseNet model took an average time of 11.96 msec by using this mechanism.

2.5. Ablation experiments

The experiments to evaluate the real-time feedback system were split into two parts. In the first experiment, the Er:YAG laser was used to drill a hole starting at the bone surface and was stopped when the bone marrow was reached. The ablation laser was set to send laser pulses at the energy of 200 mJ per pulse with a repetition rate of 4 Hz. During ablation, pressurized air was pointed to the ablation site from the side of the ablation direction (see Fig. 1(a)).

Pressurized air of 2 bar was applied to gently sweep the debris from the ablation site and prevent it from flying up to the sapphire window. Even though the air could cool down the tissue, it did not optimally prevent the tissue from carbonizing, which could appear after a few dozen laser pulses. We therefore paused the ablation laser, tissue detection, and pressurized air, and then manually sprayed water on the ablation spot whenever carbonization became visible (it was usually identifiable by blackening on the surface). Moreover, before continuing ablation, we reapplied the pressurized air to sweep the remaining sprayed water, which could deteriorate or hinder the tissue texture in the OCT images.

In the second experiment, we used a motorized linear stage to move the sample and make a 0.5 mm long line cut. The stage was set to move at a constant speed of 1 mm/s. The repetition rate and energy of the ablation laser were set similarly to the hole-ablation experiment. The OCT B-scan direction was set to be perpendicular to the ablation line. Despite that, the parallel scan was superior, and the OCT-scanning size was larger than the laser-beam size. This would result in a wavy cut, where a small-sized bone (smaller than the B-scan) will be considered as bone marrow and will not be ablated by the laser. Since peripheral heat is distributed better in line ablation than in hole ablation, carbonization is observed less often. It consequently leads to a higher ablation rate [13]. Since carbonization may nevertheless appear, we still applied similar pausing, water spraying, and air-blowing steps whenever it was noticeable. However, we only paused ablation at every endpoint of the line.

2.6. Performance evaluation

The ablated samples were evaluated radiographically with a micro computed tomography (micro-CT) (Bruker SkyScan 1275, Belgium) to obtain three-dimensional geometrical information of the ablation crater shape. The micro-CT images had a dimension of 1944 pixels in height and 1944 pixels in width. The voxel spacing of the image was 16 μm equally for both axes. The radiographical images were taken before and after cutting the sample with the laser (pre- and post-ablation). Both images were registered and overlaid to precisely identify the boundary between bone and bone marrow. We used the registration estimator application in Matlab with the monomodal intensity-based rigid registration techniques [78] to estimate the shift between the pre- and post-ablation CT images.

The evaluation of the feedback system was performed by measuring the volume and maximum depth of collateral damage (perforation) to the bone marrow. The ablation samples used for evaluation were different from the samples for training the deep-learning model. A total of six new samples were used, three of them for hole ablation and the rest for line-ablation experiments. Here, ten hole- or line-ablation experiments were made for each sample. We defined the maximum depth of perforation as the depth from the bone-bone marrow border to the bottom of the crater (illustrated as a white arrow in Fig. 6(i)). The maximum perforation depth was selected over the entire micro-CT image slice that covered the ablation crater. Furthermore, we measured the volume of the collateral damage by segmenting (with a threshold method) the damaged area on the overlaid image and summing up the segmented areas over the whole micro-CT image slices that covered the ablation crater. Similarly, the line ablation was also evaluated over the entire micro-CT image slices covering the ablation line.

3. Results and discussion

3.1. Deep-learning training and inference

Training the Densenet model took ~6.5 hours to complete with a training accuracy of 99.67 % and a validation accuracy of 96.52 %. Furthermore, the test results of the DenseNet model showed an accuracy of 96.28 %. In our previous study, the attenuation coefficient profile, which was explicitly extracted using a depth-resolved method, improved the detection accuracy. However, the time to extract this profile delayed the detection time. Other than that, we believed that our model also tried to implicitly extract the attenuation coefficient profile, but it is difficult to visualize filters over all the layers in the DenseNet model. Finally, in our current approach, both image acquisition and inference with the DenseNet model (detection time) took only 45.96 msec, which was faster than the laser's repetition rate of 4 Hz. Our feedback system can therefore be considered a real-time feedback system.

3.2. Ablation evaluation

Figure 5(a) shows an axial slice of the micro-CT image for the hole-ablation experiment. The closed-loop controlled laser system resulted in an automatic interruption of the laser beam as soon as bone marrow was detected. However, a small perforation on the bone marrow is noticeable. Statistically, the average maximum depth of perforation in 30 holes was 0.216 mm (± 0.140 mm), and the deepest measured bone marrow perforation was 0.910 mm. The average volume loss of bone marrow was 0.077 mm³ (± 0.076 mm³) with a maximum of 0.299 mm³. Figure 6(h) shows a sagittal slice of the CT image for the line-ablation experiment. Similarly, we also observed the perforation of the bone marrow. The average maximum depth of perforation in 30 ablation lines was 0.645 mm (± 0.291 mm) with a deepest measured perforation of 1.778 mm. The average volume loss of bone marrow was 0.878 mm³ (± 0.643 mm³) with a maximum of 2.269 mm³. Tables 1 and 2 show more detail of the experiment results.

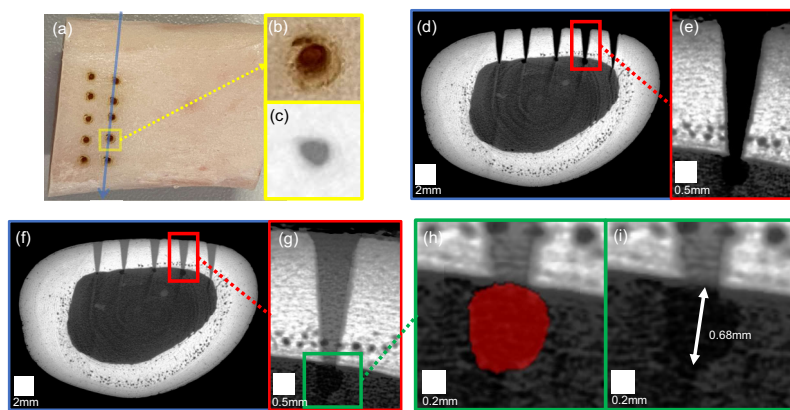


Fig. 5. An example for the hole-ablation experiment (a) with a zoomed-in image of a hole (b) and its maximum intensity projection from the micro-CT image (c). A micro-CT axial slice image for post-ablation is shown in (d) with a zoomed-in image (e) over a hole. The axial slice was taken over the blue line at (a). Similarly, image (f) shows the overlaid CT images between pre- and post-ablation of the axial slice with the zoomed version (g). Image (h) illustrates a segmented region of the bone marrow perforation (transparent red) to measure the bone marrow volume loss. Lastly, image (i) illustrates the measurement of the maximum depth perforation (white arrow) of the bone marrow.

3.3. Discussion

Ideally, clean bone surfaces free of carbonization are expected when using Er:YAG laser osteotomy if adequate water cooling is applied. In our experiments, continuous water cooling was impossible because it would have deteriorated the OCT images and limited the detection accuracy of our tissue classifier. Therefore, we manually paused the ablation and sprayed water on the ablation spot whenever carbonization was noticeable. The carbonized part of the bone quickly evaporated after rehydration and reablation sequentially. This sequence was stopped once the bone marrow was reached to prevent further damage or perforation to the bone marrow. We, therefore, expected a trace amount of carbonization. Figure 5(d) shows that a noticeable amount of carbonization appeared on the walls of the ablation craters.

In the line-ablation experiments, carbonization was less than in the hole-ablation experiments (see Fig. 6(b)). This is because the thermal dissipation was distributed better along the ablation line. However, the perforation of bone marrow in the line-ablation experiments was more than in the hole-ablation experiments. This is mainly due to the overlapping conditions at the periphery

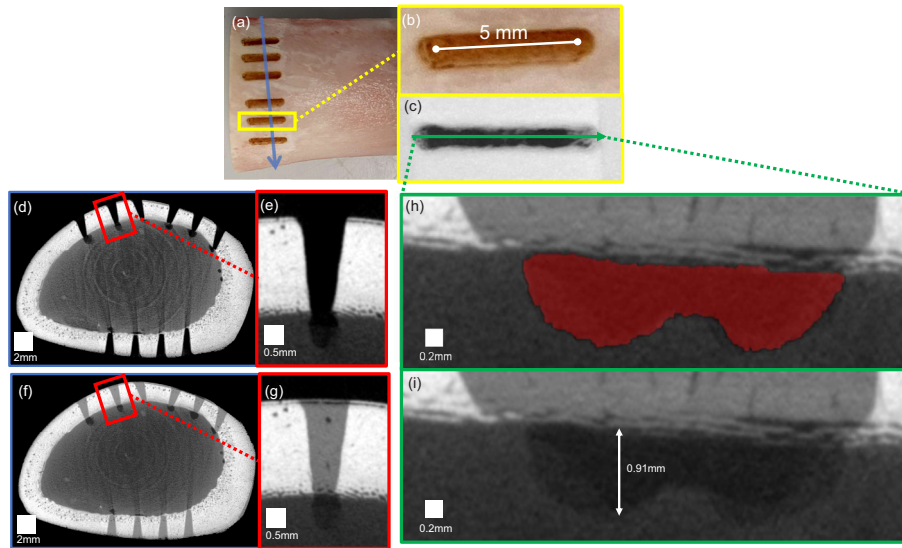


Fig. 6. An example result from the line-ablation experiment (a) with a zoomed image of the line cut (b) and its maximum intensity projection from the micro-CT images (c). A micro-CT axial slice image for post-ablation is shown in (d) with a zoomed-in image (e) over a hole. The axial slice was taken over the blue line at (a). Similarly, image (f) shows the overlaid CT images between pre- and post-ablation of the axial slice with the zoomed version (g). Image (h) shows the micro-CT sagittal slice image of the cut line and illustrates a segmented region of the bone marrow perforation (transparent red) to measure the bone marrow volume loss. Lastly, image (i) illustrates the measurement of the maximum depth perforation (white arrow) of the bone marrow.

Table 1. The measurement results for maximum perforation depth and volume loss from $N = 30$ hole-ablation experiments. The results were also compared with the pyrolysis-photoacoustic method [29,30]. Note that only the maximum perforation measurements from hole-ablation experiments are available from the reference method. The data were recalculated based on the average bone thickness of 2.9 mm.

Methods	Our method (Hole ablation)		Pyrolysis-photoacoustic [29,30]
	$N = 30$		$N = 98$
	Max perforation (mm)	Volume loss (mm ³)	Max perforation (mm)
Min	0.021	0.001	0.000
Max	0.910	0.299	0.512
Mean	0.216	0.077	0.065
Median	0.178	0.055	0.015
Std dev	0.140	0.076	0.088

of the laser beam. The intensity profile of our laser beam was close to Gaussian, with higher intensity in the middle and lower intensity on the periphery. The energy on the periphery is insufficient to ablate the bone significantly, but it is enough to ablate the bone marrow. A tophat-beam intensity profile could be ideal for osteotomy. During hole ablation, this peripheral intensity was mostly eliminated by the wall of the crater. By contrast, this peripheral beam may still ablate the adjacent point over the line during line ablation. Additionally, the OCT detection

Table 2. The measurement results for maximum perforation depth and volume loss from $N = 30$ line-ablation experiments.

Line ablation $N = 30$		
	Max perforation (mm)	Volume loss (mm ³)
Min	0.178	0.110
Max	1.778	2.269
Mean	0.645	0.878
Median	0.572	0.777
Std dev	0.291	0.643

locations were limited to the primary laser beam and could not cover the whole beam (primary and peripheral beam). Although it may be beneficial in faster bone cutting time, the damage to the bone marrow was more. Additionally, the water content in the bone marrow is higher than in bone. Bone material consists approximately 13 % water [79], while marrow tissue consists approximately between 15 - 40 % water [80]. Thus with a constant laser-pulse energy, the ablation rate in bone marrow is higher than in bone. As a result, bone marrow is easily ablated.

All experiments showed a slight perforation of bone marrow. This indicates that the deep learning always stopped the ablation whenever the bone marrow was reached and that no premature stops were made. The perforations were expected because the deep-learning model was trained based on image patches containing only a single tissue type. It was insensitive to multilayered conditions. It therefore only stopped the laser when the image patch only contained bone marrow.

Multilayered tissue detection (segmentation) would provide more accurate detection, especially at bone-bone marrow interface areas. Unfortunately, our OCT image contrast was insufficient for multilayered detection. The bone tissue scattered and absorbed most of the OCT light. Furthermore, the small signal coming from the bone marrow structure was reduced by multiple scatterings. There was therefore a large contrast difference between bone and bone marrow on multilayered tissue with bone on top. As a result, the bone marrow structure intensity appeared to be weak in the OCT images (see Fig. 7(a)) and detecting it was difficult. Figure 7(b) shows the OCT image when ablation had already reached the bone marrow. The bone marrow texture (speckle) is blurred due to frame averaging during the ablation process, which is induced by the motion of liquid materials at the surface. The liquid appears as the effect of the high-pressure explosion at the ablation center that squeezes the surrounding bone marrow and discharges liquid materials, e.g., water and liquid fat [14]. They then diffuse and cover the bone marrow surface. Furthermore, multilayered detection of bone and bone marrow on the OCT image would provide more precise control through predicting the remaining depth of the bone needed to be cut. Ideally, with such predictions, we could slow down the ablation rate or reduce the laser energy such that the cut would stop right before it touches the bone marrow. However, our laser safety mechanism prevents us from having control over increasing or reducing the laser pulse energy (ablation rate). This mechanism requires the user to stop or pause the laser from pulsing before changing any parameter of the laser pulse (repetition rate and energy). The pulsing of the laser may be continued once the repetition rate and energy are confirmed. This pausing mechanism delays the laser pulse up to around 30 seconds. Therefore, during the experiments, the laser energy was kept constant. Ablation to the bone marrow was, therefore, almost unavoidable when the bone thickness was less (still detected as bone) than the amount that would be ablated by the next laser pulse.

To summarize, the proposed real-time feedback system demonstrated to have a comparable performance to the combined pyrolysis-photoacoustic method [29,30] for hole ablation. The reference method used laser ablation alone both for ablation and as the detection light source.

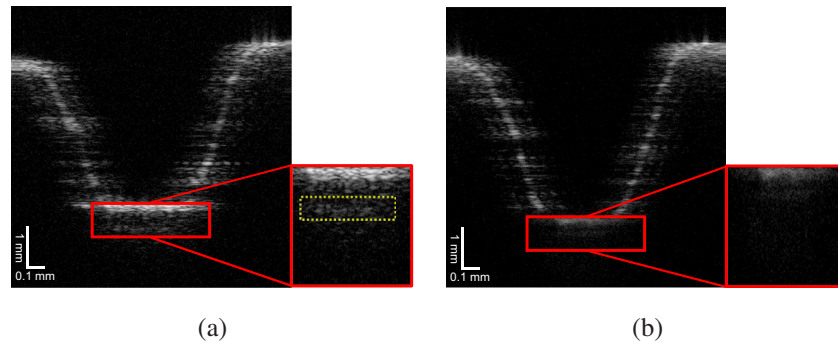


Fig. 7. OCT images during ablation with patches for tissue detection. The left image (a) shows an OCT image with two layers of tissue, bone on top and bone marrow on the bottom (dashed yellow box). The bone marrow structure intensity appears to be weak due to the high absorption of light in the bone marrow tissue. The right image (b) shows an OCT image when ablation had already reached the bone marrow.

In this situation, the detection mechanism stops together with the ablation laser once the laser reaches the bone marrow, which makes the closed-loop scenario unrepeatable. This means that the ablation and detection mechanism can only start at bone. A restart mechanism is needed once the laser beam reaches the bone marrow, after which neither ablation nor tissue-type detection can continue. The detection system has to be manually set to the default tissue type for each ablation point. By contrast, our OCT detection system runs independently from the ablation laser, which eliminates the redundant restart mechanism. And although our results show higher perforation, this approach offers a noninvasive way to monitor the ablation process. It eliminates unnecessary damage due to sensor mounting in the pyrolysis-photoacoustic method. The perforation, in our case, is also higher since we have a higher ablation rate of the Er:YAG laser. Even though perforation could not be perfectly solved with our method, we believe that it could be used as a safety feature on a laser-osteotomy system.

4. Conclusion and outlook

The first real-time feedback using OCT for laser osteotomy was demonstrated and performed comparable to the reference method [29,30]. The feedback system offers a completely noninvasive way of monitoring laser ablation. For the hole-ablation experiments, the average maximum depth of perforation and volume loss were 0.216 mm (± 0.140 mm) and 0.077 mm³ (± 0.076 mm³), respectively. On the other hand, the average maximum depth of perforation and volume loss for the line-ablation experiments were 0.645 mm (± 0.291 mm) and 0.878 mm³ (± 0.643 mm³), respectively. These results are also comparable to osteotomy with a drill that was reported to have a mean perforation of 0.660 mm [81].

These results show the feasibility of using OCT as a feedback system for laser osteotomy in the operating room. This paper provides the basic framework for tissue-specific laser osteotomy using deep-learning-assisted optical coherence tomography. Several optimizations could still be undertaken or combined with the system, such as carbonization detection, depth control, predefined ablation rate, multilayered tissue detection, and real-time control of the laser energy.

Carbonization remains a challenge in using OCT as the guidance in laser osteotomy because continuous water irrigation reduces the tissue-detection accuracy. Our pause-sequence method may partly solve this problem, but it would be better if one could detect any carbonization and sync the result to an irrigation controller. Synchronization between OCT detection and a water spray may improve this method's effectiveness.

Furthermore, several other aspects could still be optimized to improve the precision of detection and reduce the perforation depth. In ideal clinical conditions, a surgeon could plan the ablation site and depth based on a patient's CT data. The OCT system could be used as a depth-control mechanism during ablation. Concurrent tissue detection could be used as a second parameter to support the depth control in stopping the laser whenever it accidentally touches bone marrow. Nevertheless, a registration mechanism between the CT and OCT images is essential to pinpointing the surface reference for accurate depth measurements. In the future, we need to investigate the implementation of such a method to register the OCT image position relative to the CT image position and track the ablation site in real time. Additionally, this paper only demonstrated and validated the performance of real-time tissue detection using deep learning. In this way, we avoided bias in validating the performance between depth control and tissue detection.

In future work, we will also investigate multilayered tissue detection (segmentation) from OCT images. It should improve the precision of cuts by providing a prediction of the remaining bone thickness. Then control over the laser pulse energy and repetition rate could be used to slow down the ablation rate whenever the laser pulse is predicted to cut bone marrow. Such a prediction could be implemented using a Kalman filter to predict the trajectory of the ablation after the next laser pulse [82]. Nevertheless, a sufficient number of labeled ground-truth images will be needed to train the deep-learning (segmentation) model. It is a challenge to label such ground-truth images, which may involve a trained OCT image expert. Even more, it will be a challenge to label images taken during laser ablation, which alters the tissue texture in OCT images.

Funding. Werner Siemens-Stiftung (Minimally Invasive Robot-Assisted Computer-guided Laserosteotomy project).

Acknowledgments. The authors gratefully acknowledge the assistance given by Dr. Georg Schulz and his team for providing the micro-CT images.

Disclosures. The authors declare no conflicts of interest.

Data availability. The data underlying the results presented in this paper are not publicly available at this time but may be obtained from the authors upon reasonable request.

References

1. N. Jowett, W. Wöllmer, R. Reimer, J. Zustin, U. Schumacher, P. W. Wiseman, A. M. Mlynarek, A. Böttcher, C. V. Dalchow, B. B. Lörincz, R. Knecht, and R. J. D. Miller, "Bone ablation without thermal or acoustic mechanical injury via a novel picosecond infrared laser (PIRL)," *Otolaryngol. Neck Surg.* **150**(3), 385–393 (2014).
2. Y.-M. Lee, R. Y. Tu, A. Chiang, and Y.-C. Huang, "Average-power mediated ultrafast laser osteotomy using a mode-locked Nd:YVO₄ laser oscillator," *J. Biomed. Opt.* **12**(6), 060505 (2007).
3. B. Girard, K. Franjic, M. Cloutier, D. Wilson, C. Clokie, B. Wilson, and R. Miller, "Bone surgery with femtosecond laser compared to mechanical instruments: Healing studies," *Proc. SPIE* **6261**, 62612J (2006).
4. M. Ivanenko, M. Werner, S. Afilal, M. Klasing, and P. Hering, "Ablation of hard bone tissue with pulsed Co₂ lasers," *Med. Laser Appl.* **20**(1), 13–23 (2005).
5. R. Mauceri, V. Panzarella, L. Maniscalco, A. Bedogni, M. Licata, A. Albanese, F. Toia, E. Cumbo, G. Mazzola, O. Di Fede, and G. Campisi, "Conservative surgical treatment of bisphosphonate-related osteonecrosis of the jaw with Er,Cr:YsGg laser and platelet-rich plasma: a longitudinal study," *BioMed Res. Int.* **2018**, 1–10 (2018).
6. Y. Ohsugi, A. Aoki, K. Mizutani, S. Katagiri, M. Komaki, M. Noda, T. Takagi, S. Kakizaki, W. Meinzer, and Y. Izumi, "Evaluation of bone healing following Er:YAG laser ablation in rat calvaria compared with bur drilling," *J. Biophotonics* **12**(3), e201800245 (2019).
7. D. G. Panduric, I. B. Juric, S. Music, K. Molcanov, M. Susic, and I. Anic, "Morphological and ultrastructural comparative analysis of bone tissue after Er:YAG laser and surgical drill osteotomy," *Photomed. Laser Surg.* **32**(7), 401–408 (2014).
8. K.-U. Lewandrowski, C. Lorente, K. T. Schomacker, T. J. Fiotte, J. W. Wilkes, and T. F. Deutsch, "Use of the Er:YAG laser for improved plating in maxillofacial surgery: Comparison of bone healing in laser and drill osteotomies," *Lasers Surg. Med.* **19**(1), 40–45 (1996).
9. G. M. Peavy, L. Reinisch, J. T. Payne, and V. Venugopalan, "Comparison of cortical bone ablations by using infrared laser wavelengths 2.9 to 9.2 micrometer," *Lasers Surg. Med.* **25**(5), 421–434 (1999).
10. S. Stübinger, "Advances in bone surgery: the Er:YAG laser in oral surgery and implant dentistry," *Clin. cosmetic and investigational dentistry* **2**, 47–62 (2010).

11. H. Abbasi, L. Beltran, G. Rauter, R. Guzman, P. C. Cattin, and A. Zam, "Effect of cooling water on ablation in Er:YAG laserosteotome of hard bone," in *Third International Conference on Applications of Optics and Photonics*, vol. 10453 (SPIE, 2017).
12. L. Beltran, H. Abbasi, G. Rauter, N. Friederich, P. Cattin, and A. Zam, "Effect of laser pulse duration on ablation efficiency of hard bone in microseconds regime," *Proc. SPIE* **10453**, 104531S (2017).
13. L. Beltrán Bernal, F. Canbaz, A. Droneau, N. Friederich, P. Cattin, and A. Zam, "Optimizing deep bone ablation by means of a microsecond Er:YAG laser and a novel water microjet irrigation system," *Biomed. Opt. Express* **11**(12), 7253 (2020).
14. A. Vogel and V. Venugopalan, "Mechanisms of pulsed laser ablation of biological tissues," *Chem. Rev.* **103**(2), 577–644 (2003).
15. S. R. Visuri, J. T. Walsh Jr., and H. A. Wigdor, "Erbium laser ablation of dental hard tissue: Effect of water cooling," *Lasers Surg. Med.* **18**(3), 294–300 (1996).
16. M. Hohmann, D. Dörner, F. Mehari, C. Chen, M. Späth, S. Müller, H. Albrecht, F. Klämpfl, and M. Schmidt, "Investigation of random lasing as a feedback mechanism for tissue differentiation during laser surgery," *Biomed. Opt. Express* **10**(2), 807–816 (2019).
17. R. Kanawade, F. Mahari, F. Klämpfl, M. Rohde, C. Knipfer, K. Tangermann-Gerk, W. Adler, M. Schmidt, and F. Stelzle, "Qualitative tissue differentiation by analysing the intensity ratios of atomic emission lines using laser induced breakdown spectroscopy (libs): prospects for a feedback mechanism for surgical laser systems," *J. Biophotonics* **8**(1-2), 153–161 (2015).
18. F. Mehari, M. Rohde, C. Knipfer, R. Kanawade, F. Klämpfl, W. Adler, F. Stelzle, and M. Schmidt, "Laser induced breakdown spectroscopy for bone and cartilage differentiation - ex vivo study as a prospect for a laser surgery feedback mechanism," *Biomed. Opt. Express* **5**(11), 4013–4023 (2014).
19. M. Rohde, F. Mehari, F. Klämpfl, W. Adler, F.-W. Neukam, M. Schmidt, and F. Stelzle, "The differentiation of oral soft- and hard tissues using laser induced breakdown spectroscopy - a prospect for tissue specific laser surgery," *J. Biophotonics* **10**(10), 1250–1261 (2017).
20. K. Henn, G. G. Gubaidullin, J. Bongartz, J. Wahrburg, H. Roth, and M. Kunkel, "A spectroscopic approach to monitor the cut processing in pulsed laser osteotomy," *Lasers Med. Sci.* **28**(1), 87–92 (2013).
21. H. Abbasi, L. M. Beltrán Bernal, A. Hamidi, A. Droneau, F. Canbaz, R. Guzman, S. L. Jacques, P. C. Cattin, and A. Zam, "Combined nd:yag and Er:YAG lasers for real-time closed-loop tissue-specific laser osteotomy," *Biomed. Opt. Express* **11**(4), 1790 (2020).
22. F. Mehari, M. Rohde, R. Kanawade, C. Knipfer, W. Adler, F. Klämpfl, F. Stelzle, and M. Schmidt, "Investigation of the differentiation of ex vivo nerve and fat tissues using laser-induced breakdown spectroscopy (libs): Prospects for tissue-specific laser surgery," *J. Biophotonics* **9**(10), 1021–1032 (2016).
23. H. Abbasi, G. Rauter, R. Guzman, P. C. Cattin, and A. Zam, "Laser-induced breakdown spectroscopy as a potential tool for autocarbonization detection in laserosteotomy," *J. Biomed. Opt.* **23**(7), 1–7 (2018).
24. B. Lengenfelder, F. Mehari, M. Hohmann, M. Heinlein, E. Chelales, M. J. Waldner, F. Klämpfl, Z. Zalevsky, and M. Schmidt, "Remote photoacoustic sensing using speckle-analysis," *Sci. Rep.* **9**(1), 1057 (2019).
25. B. Lengenfelder, F. Mehari, M. Hohmann, C. Löhr, M. J. Waldner, M. Schmidt, Z. Zalevsky, and F. Klämpfl, "Contact-free endoscopic photoacoustic sensing using speckle analysis," *J. Biophotonics* **12**(12), e201900130 (2019).
26. H. Nguendon Kenhagho, G. Rauter, R. Guzman, P. C. Cattin, and A. Zam, "Optoacoustic tissue differentiation using a mach-zehnder interferometer," *IEEE Trans. Ultrason., Ferroelect., Freq. Contr.* **66**(9), 1435–1443 (2019).
27. H. Nguendon Kenhagho, S. Shevchik, F. Saeidi, N. Faivre, B. Meylan, G. Rauter, R. Guzman, P. Cattin, K. Wasmer, and A. Zam, "Characterization of ablated bone and muscle for long-pulsed laser ablation in dry and wet conditions," *Materials* **12**(8), 1338 (2019).
28. H. Nguendon Kenhagho, F. Canbaz, T. E. Gomez Alvarez-Arenas, R. Guzman, P. Cattin, and A. Zam, "Machine learning-based optoacoustic tissue classification method for laser osteotomes using an air-coupled transducer," *Lasers Surg. Med.* **53**(3), 377–389 (2021).
29. S. Rupprecht, K. Tangermann-Gerk, J. Wiltfang, F. W. Neukam, and A. Schlegel, "Sensor-based laser ablation for tissue specific cutting: an experimental study," *Lasers Med. Sci.* **19**(2), 81–88 (2004).
30. S. Rupprecht, K. Tangermann, P. Kessler, F. W. Neukam, and J. Wiltfang, "Er:yag laser osteotomy directed by sensor controlled systems," *J. Cranio-Maxillofacial Surg.* **31**(6), 337–342 (2003).
31. A. S. Novikov, I. Usenov, D. Schweda, P. Caffier, B. Limmer, V. Artyushenko, and H. J. Eichler, "Pyrometry with flexible infrared fibers for temperature-controlled laser surgery," *Biomed. Opt. Express* **13**(2), 744–760 (2022).
32. L. A. Reisner, B. W. King, M. D. Klein, G. W. Auner, and A. K. Pandya, "A prototype biosensor-integrated image-guided surgery system," *Int. J. Med. Robotics Comput. Assist. Surg.* **3**(1), 82–88 (2007).
33. P. C. Ashok, M. E. Giardini, K. Dholakia, and W. Sibbett, "A raman spectroscopy bio-sensor for tissue discrimination in surgical robotics," *J. Biophotonics* **7**(1-2), 103–109 (2014).
34. F. Stelzle, C. Knipfer, W. Adler, M. Rohde, N. Oetter, E. Nkenke, M. Schmidt, and K. Tangermann-Gerk, "Tissue discrimination by uncorrected autofluorescence spectra: A proof-of-principle study for tissue-specific laser surgery," *Sensors* **13**(10), 13717–13731 (2013).
35. A. Zam, "Optical tissue differentiation for sensor-controlled tissue-specific laser surgery," doctoral thesis, Friedrich-Alexander-Universität Erlangen-Nürnberg (FAU) (2011).

36. R. Gunaratne, I. Monteath, J. Goncalves, R. Sheh, C. N. Ironside, M. Kapfer, R. Chipper, B. Robertson, R. Khan, and D. Fick, "Machine learning classification of human joint tissue from diffuse reflectance spectroscopy data," *Biomed. Opt. Express* **10**(8), 3889–3898 (2019).
37. A. Zam, F. Stelzle, K. Tangermann-Gerk, W. Adler, E. Nkenke, F. W. Neukam, M. Schmidt, and A. Douplik, "In vivo soft tissue differentiation by diffuse reflectance spectroscopy: preliminary results," *Phys. Procedia* **5**, 655–658 (2010).
38. F. Stelzle, A. Zam, W. Adler, K. Tangermann-Gerk, A. Douplik, E. Nkenke, and M. Schmidt, "Optical nerve detection by diffuse reflectance spectroscopy for feedback controlled oral and maxillofacial laser surgery," *J. Transl. Med.* **9**(1), 20 (2011).
39. F. Stelzle, K. Tangermann-Gerk, W. Adler, A. Zam, M. Schmidt, A. Douplik, and E. Nkenke, "Diffuse reflectance spectroscopy for optical soft tissue differentiation as remote feedback control for tissue-specific laser surgery," *Lasers Surg. Med.* **42**(4), 319–325 (2010).
40. M. E. Brezinski, G. J. Tearney, B. E. Bouma, J. A. Izatt, M. R. Hee, E. A. Swanson, J. F. Southern, and J. G. Fujimoto, "Optical coherence tomography for optical biopsy," *Circulation* **93**(6), 1206–1213 (1996).
41. J. G. Fujimoto, C. Pitris, S. A. Boppart, and M. E. Brezinski, "Optical coherence tomography: An emerging technology for biomedical imaging and optical biopsy," *Neoplasia* **2**(1-2), 9–25 (2000).
42. A. Hamidi, Y. A. Bayhaqi, F. Canbaz, A. A. Navarini, P. C. Cattin, and A. Zam, "Long-range optical coherence tomography with extended depth-of-focus: a visual feedback system for smart laser osteotomy," *Biomed. Opt. Express* **12**(4), 2118–2133 (2021).
43. J. Fujimoto and W. Drexler, *Introduction to Optical Coherence Tomography* (Springer Berlin Heidelberg, 2008), pp. 1–45.
44. O. Müller, S. Donner, T. Klinder, R. Dragon, I. Bartsch, F. Witte, A. Krüger, A. Heisterkamp, and B. Rosenhahn, "Model based 3d segmentation and oct image undistortion of percutaneous implants," in *Medical Image Computing and Computer-Assisted Intervention – MICCAI 2011*, G. Fichtinger, A. Martel, and T. Peters, eds. (Springer Berlin Heidelberg, Berlin, Heidelberg, 2011), pp. 454–462.
45. D. C. Fernandez, "Delineating fluid-filled region boundaries in optical coherence tomography images of the retina," *IEEE Trans. Med. Imaging* **24**(8), 929–945 (2005).
46. C. A. Puliafito, M. R. Hee, C. P. Lin, E. Reichel, J. S. Schuman, J. S. Duker, J. A. Izatt, E. A. Swanson, and J. G. Fujimoto, "Imaging of macular diseases with optical coherence tomography," *Ophthalmology* **102**(2), 217–229 (1995).
47. G. J. Ughi, T. Adriaenssens, P. Sinnaeve, W. Desmet, and J. D'hooge, "Automated tissue characterization of in vivo atherosclerotic plaques by intravascular optical coherence tomography images," *Biomed. Opt. Express* **4**(7), 1014–1030 (2013).
48. S. Liu, Y. Sotomi, J. Eggermont, G. Nakazawa, S. Torii, T. Ijichi, Y. Onuma, P. W. Serruys, B. P. F. Lelieveldt, and J. Dijkstra, "Tissue characterization with depth-resolved attenuation coefficient and backscatter term in intravascular optical coherence tomography images," *J. Biomed. Opt.* **22**(09), 1 (2017).
49. L. S. Athanasiou, C. V. Bourantas, G. Rigas, A. I. Sakellarios, T. P. Exarchos, P. K. Siogkas, A. Ricciardi, K. K. Naka, M. I. Papafaklis, L. K. Michalis, F. Prati, and D. I. Fotiadis, "Methodology for fully automated segmentation and plaque characterization in intracoronary optical coherence tomography images," *J. Biomed. Opt.* **19**(2), 026009 (2014).
50. J. Yang, B. Zhang, H. Wang, F. Lin, Y. Han, and X. Liu, "Automated characterization and classification of coronary atherosclerotic plaques for intravascular optical coherence tomography," *Biocybern. Biomed. Eng.* **39**(3), 719–727 (2019).
51. J. J. Rico-Jimenez, D. U. Campos-Delgado, M. Villiger, K. Otsuka, B. E. Bouma, and J. A. Jo, "Automatic classification of atherosclerotic plaques imaged with intravascular oct," *Biomed. Opt. Express* **7**(10), 4069–4085 (2016).
52. N. Katta, A. D. Estrada, A. B. McElroy, A. Gruslova, M. Oglesby, A. G. Cabe, M. D. Feldman, R. D. Fleming, A. J. Brenner, and T. E. Milner, "Laser brain cancer surgery in a xenograft model guided by optical coherence tomography," *Theranostics* **9**(12), 3555–3564 (2019).
53. Y. Fan, B. Zhang, W. Chang, X. Zhang, and H. Liao, "A novel integration of spectral-domain optical-coherence-tomography and laser-ablation system for precision treatment," *International Journal of Computer Assisted Radiology and Surgery* **13**(3), 411–423 (2018).
54. Y. Zhang, T. Pfeiffer, M. Weller, W. Wieser, R. Huber, J. Raczowsky, J. Schipper, H. Wörn, and T. Klenzner, "Optical coherence tomography guided laser cochleostomy: Towards the accuracy on tens of micrometer scale," *BioMed Res. Int.* **2014**, 1–10 (2014).
55. J. D. Díaz, D. Kundrat, K.-F. Goh, O. Majdani, and T. Ortmaier, *Towards Intra-operative OCT Guidance for Automatic Head Surgery: First Experimental Results* (Lecture Notes in Computer Science, 2013), p. 347–354.
56. A. Fuchs, M. Schultz, A. Krüger, D. Kundrat, J. D. Díaz, and T. Ortmaier, "Online measurement and evaluation of the Er:YAG laser ablation process using an integrated OCT system," *Biomedical Engineering/Biomedizinische Technik* **57**(SI-1 Track-H), 434–437 (2012).
57. J. Jivraj, C. Chen, Y. Huang, J. Ramjani, Y. Lu, B. Vuong, X. Gu, and V. X. D. Yang, "Smart laser osteotomy: integrating a pulsed 1064nm fiber laser into the sample arm of a fiber optic 1310nm OCT system for ablation monitoring," *Biomed. Opt. Express* **9**(12), 6374–6387 (2018).

58. B. Y. Leung, P. J. Webster, J. M. Fraser, and V. X. Yang, "Real-time guidance of thermal and ultrashort pulsed laser ablation in hard tissue using inline coherent imaging," *Lasers Surg. Med.* **44**(3), 249–256 (2012).
59. F.-Y. Chang, M.-T. Tsai, Z.-Y. Wang, C.-K. Chi, C.-K. Lee, C.-H. Yang, M.-C. Chan, and Y.-J. Lee, "Optical coherence tomography-guided laser microsurgery for blood coagulation with continuous-wave laser diode," *Sci. Rep.* **5**(1), 16739 (2015).
60. H. H. Müller, L. Ptaszynski, K. Schlott, C. Debbeler, M. Bever, S. Koinzer, R. Birngruber, R. Brinkmann, and G. Hüttmann, "Imaging thermal expansion and retinal tissue changes during photocoagulation by high speed OCT," *Biomed. Opt. Express* **3**(5), 1025–1046 (2012).
61. A. Hamidi, Y. A. Bayhaqi, F. Canbaz, A. Navarini, P. C. Cattin, and A. Zam, "Imaging photothermal-induced expansion of bone during laser osteotomy by phase-sensitive OCT: preliminary results," *Proc. SPIE* **11359**, 113590K (2020).
62. "CUDA Toolkit Documentation," <https://docs.nvidia.com/cuda/>. Accessed: 2020-09-30.
63. D. M. S. Barros, J. C. C. Moura, C. R. Freire, A. C. Taleb, R. A. M. Valentim, and P. S. G. Morais, "Machine learning applied to retinal image processing for glaucoma detection: review and perspective," *BioMedical Engineering OnLine* **19**(1), 20 (2020).
64. J. Möller, A. Bartsch, M. Lenz, I. Tischoff, R. Krug, H. Welp, M. R. Hofmann, K. Schmieder, and D. Miller, "Applying machine learning to optical coherence tomography images for automated tissue classification in brain metastases," *Int. J. Comput. Assist. Radiol. Surg.* **16**(9), 1517–1526 (2021).
65. I. Goodfellow, Y. Bengio, and A. Courville, *Deep Learning* (MIT Press, 2016). <http://www.deeplearningbook.org>.
66. O. A. Montesinos López, A. Montesinos López, and J. Crossa, *Convolutional Neural Networks* (Springer International Publishing, 2022), pp. 533–577.
67. A. G. Roy, S. Conjeti, S. P. K. Karri, D. Sheet, A. Katouzian, C. Wachinger, and N. Navab, "Relaynet: retinal layer and fluid segmentation of macular optical coherence tomography using fully convolutional networks," *Biomed. Opt. Express* **8**(8), 3627–3642 (2017).
68. S. Borkovkina, A. Camino, W. Janponsri, M. V. Sarunic, and Y. Jian, "Real-time retinal layer segmentation of OCT volumes with GPU accelerated inferencing using a compressed, low-latency neural network," *Biomed. Opt. Express* **11**(7), 3968–3984 (2020).
69. Y. A. Bayhaqi, A. Hamidi, F. Canbaz, A. A. Navarini, P. C. Cattin, and A. Zam, "Deep learning models comparison for tissue classification using optical coherence tomography images: toward smart laser osteotomy," *OSA Continuum* **4**(9), 2510–2526 (2021).
70. K. Simonyan and A. Zisserman, "Very deep convolutional networks for large-scale image recognition," in *3rd International Conference on Learning Representations, ICLR 2015*, Y. Bengio and Y. LeCun, eds. (2015).
71. K. He, X. Zhang, S. Ren, and J. Sun, "Identity mappings in deep residual networks," in *Computer Vision - ECCV 2016*, B. Leibe, J. Matas, N. Sebe, and M. Welling, eds. (Springer International Publishing, 2016), pp. 630–645.
72. G. Huang, Z. Liu, L. V. D. Maaten, and K. Q. Weinberger, "Densely connected convolutional networks," in *2017 IEEE Conference on Computer Vision and Pattern Recognition (CVPR)*, (2017), pp. 2261–2269.
73. J. Canny, "A computational approach to edge detection," *IEEE Trans. Pattern Anal. Mach. Intell.* **PAMI-8**(6), 679–698 (1986).
74. S. Luo, J. Yang, Q. Gao, S. Zhou, and C. A. Zhan, "The edge detectors suitable for retinal OCT image segmentation," *J. Healthcare Eng.* **2017**, 1–13 (2017).
75. A. Paszke, S. Gross, and F. Massa, *et al.*, "Pytorch: An imperative style, high-performance deep learning library," in *Advances in Neural Information Processing Systems 32*, (Curran Associates, Inc., 2019), pp. 8024–8035.
76. "Open Neural Network Exchange," <https://onnx.ai/>. Accessed: 2020-09-30.
77. "NVIDIA TensorRT," <https://developer.nvidia.com/tensorrt>. Accessed: 2020-09-30.
78. "Matlab: Registration Estimator App," <https://ch.mathworks.com/help/images/approaches-to-registering-images.html>. Accessed: 2020-09-30.
79. M. Forrer, M. Frenz, V. Romano, H. Altermatt, H. Weber, A. Silenok, M. Istomyn, and V. Konov, "Bone-ablation mechanism using co 2 lasers of different pulse duration and wavelength," *Appl. Phys. B* **56**(2), 104–112 (1993).
80. T. Aoki, S. Yamaguchi, S. Kinoshita, Y. Hayashida, and Y. Korogi, "Quantification of bone marrow fat content using iterative decomposition of water and fat with echo asymmetry and least-squares estimation (ideal): reproducibility, site variation and correlation with age and menopause," *The Br. J. Radiol.* **89**(1065), 20150538 (2016).
81. Y. Hsu, S. Lee, and H. Lin, "A modular mechatronic system for automatic bone drilling," *Biomed. Eng. - Appl. Basis Commun.* **13**(04), 168–174 (2001).
82. Kalman filtered depth prediction using Optical Coherence Tomography for laser bone cutting, Zenodo, 2021, <https://doi.org/10.5281/zenodo.4922992>.